ACS OMEGA

http://pubs.acs.org/journal/acsodf

Article

Multiphase Flow Characteristics in the Classification Process of a Novel Wide Neck Thickener: Experiment and Simulation

Yan Zheng, Fanfei Min,* and Chuanzhen Wang

Cite This: *ACS Omega* 2022, 7, 38660−38673

Read Online

ACCESS | Metrics & More | Article Recommendations

ABSTRACT: A novel thickening equipment known as a wide neck thickener (WNT) was designed to solve the problem of depending only on gravity settlement of the thickener. The computational fluid dynamics method with the Reynolds stress and the volume of fluid models and the particle image velocimetry experimental method were both applied to investigate the pressure and velocity variation and turbulent characteristics of the WNT under different parameter settings. The results indicate that experiments and simulations are consistent. Under four parameter settings, the axial and tangential velocities decrease to the minimum and then increase from the wall to the center. Under different feed velocity, cone angle, and spigot diameter settings, turbulent kinetic energy k and intensity I decrease from the cylinder to the cone and from the wall to the center; the max k and I correspond to the area near the inlet followed by the cylinder, and k and I in the cone are the smallest. When the classification overflow outlet (COO) diameter is 200 mm, k and I increase rapidly, the max k and I are transferred from near the inlet to near the cylinder wall at the COO, and the k and I near the wall decrease significantly.

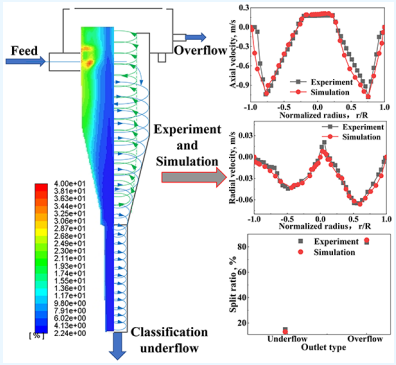

INTRODUCTION

Thickeners are important units for water recovery[1] in which particles settle under gravity to achieve solid−liquid separation.[2−4] This process has been widely used in many industries, such as wastewater treatment, metallurgy plants, and mineral processing.[5−10] Fine minerals have low settling rates,[11] and, in order to effect faster settling, a flocculant is often added to the feed slurry and mixed to bind dispersed fine particles into larger aggregates,[12−16] this produces a clear liquor overflow and a concentrated underflow suspension of solids.[17] These suspended solids are discharged from the bottom while the clarified liquid is collected at the peripheral overflow for reuse or further purification.[1,2] However, thickeners cannot cope with the increasing number of fine minerals in the feed ore,[18] and researchers have studied the influence of various parameters on thickener performance. At the same time, due to the complexity of turbulence in the thickener, the computational fluid dynamics (CFD) method is considered as a valuable means of flow field simulation and an invaluable tool to achieve better performance of thickeners.[9,19]

Ebrahimzadeh et al.[1,20] simulated a semi-industrial pilot plant thickener based on the CFD method to evaluate the effect of important parameters on thickener performance. Burger et al.[1] predicted the performance of a series of designed feedwells, and determined the effects of the turbulence levels, flocculent type, and dosage on the flocculation kinetics in a pipe reactor based on CFD modeling. Then Kahane et al.[13] applied CFD modeling to improve the full-scale thickener performance at Worsley Alumina Limited (Collie, WA, Australia). White et al.[9] predicted the velocity fields by calculating the fluid flow in model feedwells based on the Reynolds stress model (RSM) model. Wang et al.[21] used CFD based on the RSM turbulence model to simulate the thickening process of tailings slurry in a gravity thickener, focusing on the influence of feed velocity, and the results implied that increasing the feed velocity can enhance kinetic energy dissipation performance within a certain range of feed velocity. Peloquin et al.[22] studied the influence of average particle size, feed flow rate, and inlet diameter on the flow pattern in a smaller diameter bauxite residue thickener based on CFD. Wu et al.[23] studied the flocculation sedimentation and concentration characteristics of a deep cone concentrator by CFD, and analyzed the effects of rake speed, feed velocity, and tailings slurry concentration on concentration performance. Ruan et al.[24] used CFD to simulate the flocculation and sedimentation process of whole-tailings in a deep cone thickener, and the density distribution and turbulent kinetic energy distribution were obtained. Zhou et al.[25] used CFD to acquire the flow patterns and velocity and concentration fields to investigate the settling behavior of red mud in an industrial scale thickener. Banisi et al.[26] established a model using CFD and studied the

Received: July 2, 2022
Accepted: October 4, 2022
Published: October 17, 2022

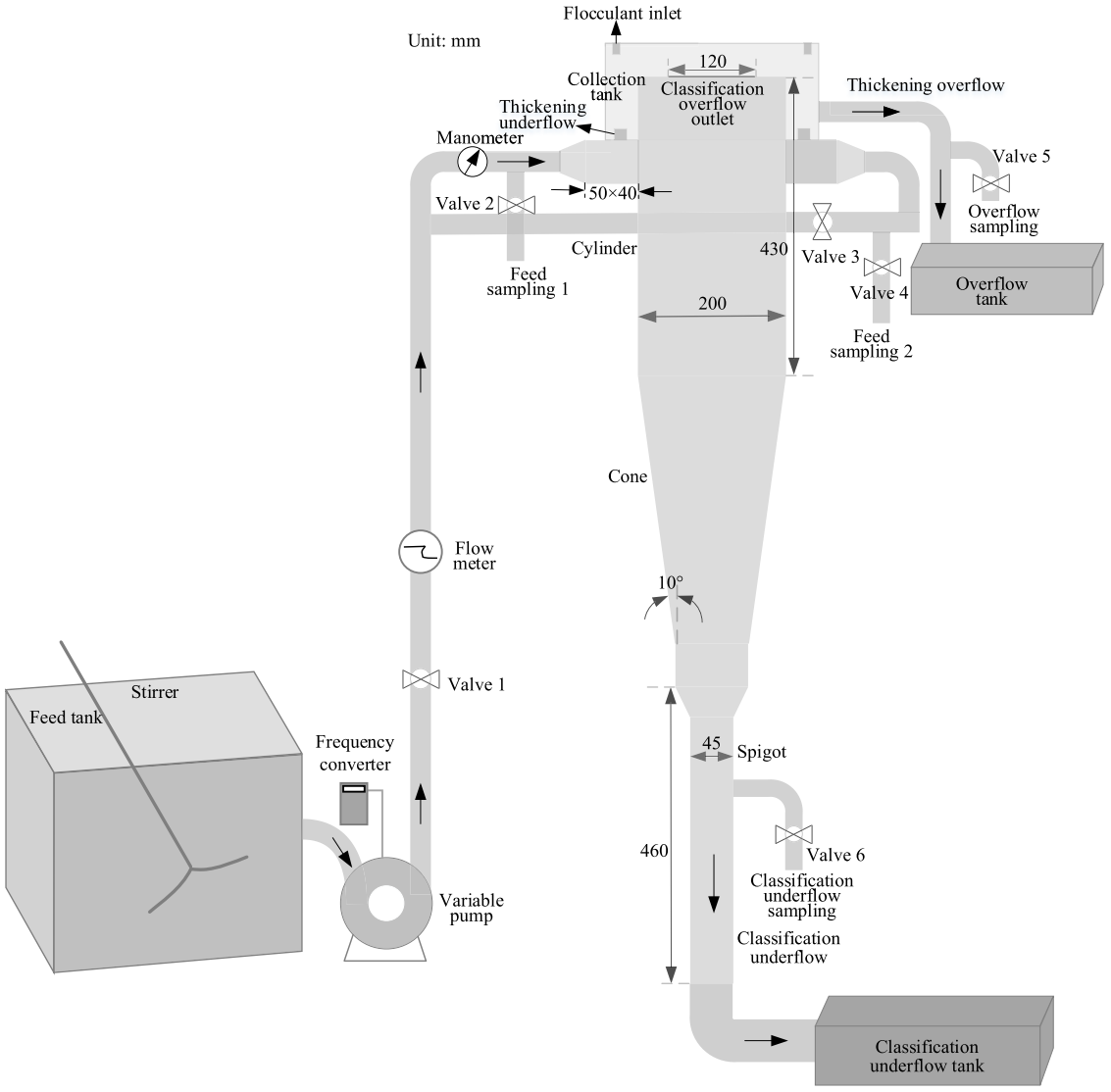

Figure 1. Schematic and parameters of the WNT.

performance of the thickener by utilizing a feeding system that effectively dissipated the energy of the feed stream, as well as the way of adding flocculants in stages. Aashranth et al.[27] used CFD to simulate the disengagement process and predict the solid phase volume fraction at different heights of the continuous thickener. Zhou et al.[28] used CFD to obtain the residence-time distribution and compartment model to study the flow characteristics of red mud separation thickener's feedwells. Tanguay et al.[29] used CFD to study the influence of the flocculation process on the flow field and the effects of the internal aggregate structure on the flocculation performance of the feedwell. The research of Fawell et al.[30] indicated that CFD can be used to identify changes in design elements or operating conditions of the thickener to improve the performance of its feedwell. Wang et al.[31] used CFD to investigate the momentum and turbulent dissipation rate of the feedwell at various feed velocities, and discussed the influence of flow characteristics on flocculation performance. Stephens et al.[32] discussed and demonstrated the application of CFD models for flocculant adsorption in an industrial thickener. Owen et al.[33] studied the effects of inlet direction and velocity on the solid−liquid separation of tailings slurry in a gravity thickener by using feedwell CFD.

Although many achievements have been made in the research of thickener performance, most current studies are based on the central feeding mode of traditional thickeners, and minerals in thickeners depend only on gravity settlement and the settling speed is slow. Changing the feeding mode to realize the combination of classification and settlement has not been considered. Therefore, a novel thickening mechanism known as wide neck thickener (WNT) was proposed in this study, and a tangential centrifugal force was introduced. WNT integrates classification and thickening sedimentation to reduce the sedimentation area of the equipment and improve the efficiency of classification and thickening sedimentation. The parameters affecting the performance of thickeners include feed flow rate, feed solid concentration, particle size, and flocculant dosage.[34] At the same time, due to the similarity between the geometric structure of the classification process and the traditional hydrocyclone, the main structural parameters include overflow outlet diameter,[35] cone angle, and underflow outlet diameter.[36] Combined with the influencing parameters of thickener and hydrocyclone, four parameters (feed velocity, classification

https://doi.org/10.1021/acsomega.2c04168
ACS Omega 2022, 7, 38660−38673

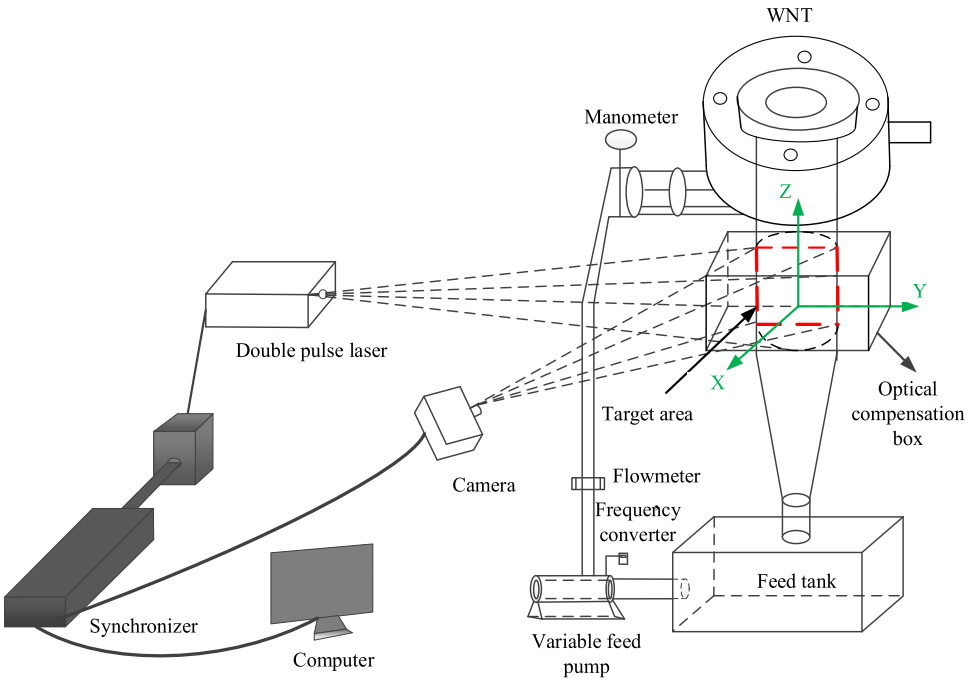

Figure 2. Principle of PIV measurement.

overflow outlet (COO) diameter, cone angle, and spigot diameter) were studied in this paper to provide the basis for WNT design. Added to this, Wang and Yu,[37] Xu,[36] and Zhang et al.[38] studied the hydrocyclone dimension effects on a multiphase flow with the RSM turbulence and volume of fluid (VOF) multiphase models in CFD. Therefore, the CFD method with RSM turbulence and VOF multiphase models was used in this study.

The fluid flow characteristics of WNT have a crucial impact on classification. Aiming to verify the reliability of the simulation results, particle image velocimetry (PIV) test was also performed to explore the fluid flow of WNT. Therefore, the study adopts the research method of combining physical experiments and numerical simulations to explore the fluid flow of WNT. The objectives of the present work can be described as follows:

(1) Describe the development process and velocity distribution of the flow field in the WNT under different parameter settings via the simulation and PIV experiment methods.

(2) Analyze the turbulent kinetic energy k, intensity I, and dissipation rate ε to obtain the turbulent characteristics.

METHODOLOGY

WNT. The schematic and parameters as shown in Figure 1 have been used for the studies of the performance characteristics of WNT. The WNT includes classification and thickening processes. The classification process includes a tangential feed inlet, a classification underflow outlet (CUO) at the bottom for discharging coarse minerals, and a COO at the top for discharging fine minerals. The collection tank is closed at the top of the WNT. When minerals enter the WNT along the tangential inlet at a speed, minerals rotate outward along the wall of the cylindrical section to the conical section under the joint action of centrifugal force, gravity, and resistance. In the conical section, some fine minerals are separated from the external swirl by the inward drag force and rotated upward to form classification overflow, and other minerals flow out from the CUO. In the thickening process, a flocculant is added from the top of the collection tank and mixed with the classification overflow collected in the collection tank. Then the flocculated minerals are discharged from the thickening underflow outlet, and the clarified liquid is discharged from the thickening overflow outlet. This paper mainly studies the classification process of the WNT.

In traditional thickeners, minerals are flocculated and settled by adding flocculants. Minerals with different particle sizes have different flocculation and sedimentation effects, and the use effect of flocculants cannot be guaranteed. However, the WNT can first realize the classification settlement of minerals, larger minerals flow out from the CUO, and most fine minerals flow out from the COO, avoiding the mixed settlement of multiple mineral sizes. The fine minerals flowing out from the COO can achieve flocculation settlement by adding flocculants, which is beneficial to improving the utilization efficiency of flocculants. At the same time, the turbulent intensity at the COO is large, and after adding the flocculant, the flocculant is mixed with the fine minerals without stirring.

Experimental Apparatus. The equipment shown in Figure 1 mainly includes a feed tank of 0.18 m^3, a variable pump of 0−30 m^3/h, a frequency converter of 0−50 Hz, and a WNT. The feed pressure and mass flow are measured by a manometer and a flowmeter, respectively. A section of the optical compensation box under the inlet in the WNT is filled with water to weaken the light refraction from the cylindrical column. Both the WNT and the optical compensation box are made of Plexiglas with excellent optical transparency. The principle of PIV measurement is shown in Figure 2.

The experimental procedure of PIV measurement in the WNT can be described as follows. First, a high-definition camera (type: ICL-B2520M-SC000, IMPERX) was placed at 0.265 m in front of the optical compensation box, and then the lens was focused on the WNT (see the red dotted rectangle in Figure 2) for clear camera shooting. The camera was equipped with a

https://doi.org/10.1021/acsomega.2c04168
ACS Omega 2022, 7, 38660−38673

Nikon 50 mm f/1.8 lens for a resolution of 2456 × 2058 pixels and a max exposure frequency of 20 Hz. Afterward, deionized water can flow from the inlet to the WNT. In this study, the feed velocity was 2 m/s for comparison with the numerical simulation under the same feed velocity. Meanwhile, the classification underflow and the classification overflow were obtained. Finally, the evolution process of the flow field in the WNT can be recorded by the camera.

Structured Grid. The flow field geometric model of the WNT was established through the geometry function module of Integrated Computational Engineering and Manufacturing 2019 (ICEM 19.0), the flow field was divided into structured grids, and the corresponding mesh files were generated (see Figure 1).

The grid independence test is a necessary part of CFD simulation. Here, additional simulation conditions were kept unadjusted, and the simulated flow field had different grid numbers. These discrete results were then compared and analyzed for changes occurring under different grid densities. If the simulation results do not alter with the number of grids or change very little, it can be considered that the simulation grid is independent. The CFD results of three different grid structure densities of WNT were compared. The information in Table 1

Table 1. Grid Information of the Flow Field Model

	structured grid density		
	fine	medium	coarse
total elements	985,068	494,720	248,107
minimum of determination	0.8	0.8	0.7
maximum of cell skewness	0.8	0.8	0.8

illustrates three grid densities, and adopts the minimum of determination and maximum of cell skewness as average indices of grid quality. Their values are less than 0.8 and greater than 0.7, respectively.

Numerical Model. In this study, the size of the WNT assembly in CFD simulation is consistent with that in the experiment (Figure 1). The combination of the VOF[39] and the RSM[40,41] was used to describe the fluid flow in the WNT. The VOF model serves to characterize the liquid−gas two-phase fluid using water and air in the WNT, as shown in eqs 1−3.

$$\frac{1}{\rho_q}\left[\frac{\partial}{\partial t}(\alpha_q\rho_q) + \nabla\cdot(\alpha_q\rho_q\overrightarrow{u_q})\right] = \sum_{p=1}^{n}(\dot{m}_{pq} - \dot{m}_{qp}) \tag{1}$$

$$\sum_{q=1}^{n}\alpha_q = 1 \tag{2}$$

$$\frac{\partial}{\partial t}(\rho\vec{v}) + \nabla\cdot(\rho\vec{v}\vec{v}) = -\nabla p + \mu(\nabla\vec{v} + \nabla\vec{v}^{T}) + \rho\vec{g} + \vec{F} \tag{3}$$

where α_q indicates the volume fraction of phase q in the computing cell; $m_{pq}\bullet(m_{qp}\bullet)$ is the mass transfer from phase $p(q)$ to phase q (p); $\vec{u}_q$ and $\vec{v}$ represent the velocity vectors (m/s); ρ_q is the density of phase q; ∇ is the Hamiltonian; p is the fluid pressure, and $\vec{F}$ denotes the Saffman lift force, virtual mass force, and pressure gradient force.

The control equations of the RSM turbulence model[40] are as follows.

Continuity equation:

$$\frac{\partial\rho}{\partial t} + \frac{\partial}{\partial x_i}(\rho u_i) = 0 \tag{4}$$

Momentum equation:

$$\frac{\partial}{\partial t}(\rho u_i) + \frac{\partial}{\partial x_i}(\rho u_i u_j) = -\frac{\partial p}{\partial x_i} + \frac{\partial}{\partial x_j}\left[\mu\left(\frac{\partial u_i}{\partial x_j} + \frac{\partial u_j}{\partial x_i}\right)\right] + \frac{\partial}{\partial x_j}(-\rho\overline{u_i'u_j'}) \tag{5}$$

$$u_i = \overline{u_i} + u_i' \tag{6}$$

Transport equations of RSM:

$$\frac{\partial}{\partial t}(\rho\overline{u_i'u_j'}) + \frac{\partial}{\partial x_k}(\rho u_k\overline{u_i'u_j'}) = \underbrace{-\frac{\partial}{\partial x_k}[\rho\overline{u_i'u_j'u_k'} + \overline{p'(\delta_{kj}u_i' + \delta_{ik}u_j')}]}_{D_{T,ij}} \underbrace{-\rho\left(\overline{u_i'u_k'}\frac{\partial u_j}{\partial x_k} + \overline{u_j'u_k'}\frac{\partial u_i}{\partial x_k}\right)}_{P_{ij}} + \underbrace{p'\left(\frac{\partial u_i'}{\partial x_j} + \frac{\partial u_j'}{\partial x_i}\right)}_{\Phi_{ij}} \underbrace{- 2\mu\overline{\frac{\partial u_i'}{\partial x_k}\frac{\partial u_j'}{\partial x_k}}}_{\varepsilon_{ij}} \tag{7}$$

where the subscript i, j, and k mean the x, y, and z components in the Cartesian coordinate system, respectively; $\overline{u}_i$ and u_i' represent the mean velocity component (m/s) and fluctuation velocity component (m/s), respectively; x_i, x_j, and x_k are the fluid position (m); ρ is the density (kg/m^3). $D_{T,ij}$ represents turbulent diffusion term; P_{ij} stands for the pressure generation term; Φ_{ij} denotes the pressure strain term and $\varepsilon_{ij}$is the dissipative term.

In addition, the standard wall function[40] was employed to model the velocity in the near-wall region, and the computing formula is shown in eq 8:

$$\frac{1}{0.4187}\ln\left(9.793\frac{\rho 0.09^{1/4}k_p^{1/2}y_p}{\mu}\right) = \frac{\rho U_p 0.09^{1/4}k_p^{1/2}}{\tau_w} \tag{8}$$

where k_P is the turbulent kinetic energy at the wall-adjacent cell centroid of P; y_P is the distance from the centroid of the wall-adjacent cell to the wall of P, and μ is the dynamic viscosity (N.s/m^2), U_P represents the mean velocity of the fluid at the wall-adjacent cell centroid of P, and τ_w is the wall shear stress.

The flow pattern of the flow field is judged by the Reynolds number of fluid (Re_f),[42] as shown in eq 9.

$$Re_f = \frac{d_f\rho_f u_f}{\mu} \tag{9}$$

where d_f is the characteristic length of the flow field (m), i.e., the hydraulic diameter of the inlet. ρ_f is the fluid density (kg/m^3), u_f represents the characteristic velocity of fluid (m/s), that is, the feed velocity. μ is the dynamic viscosity of the fluid (N·s/m^2).

The commonly used parameters to characterize fluid turbulent performance are turbulent intensity I (%), turbulent kinetic energy k (m^2/s^2), and turbulent dissipation rate ε (m^2/

https://doi.org/10.1021/acsomega.2c04168
ACS Omega 2022, 7, 38660−38673

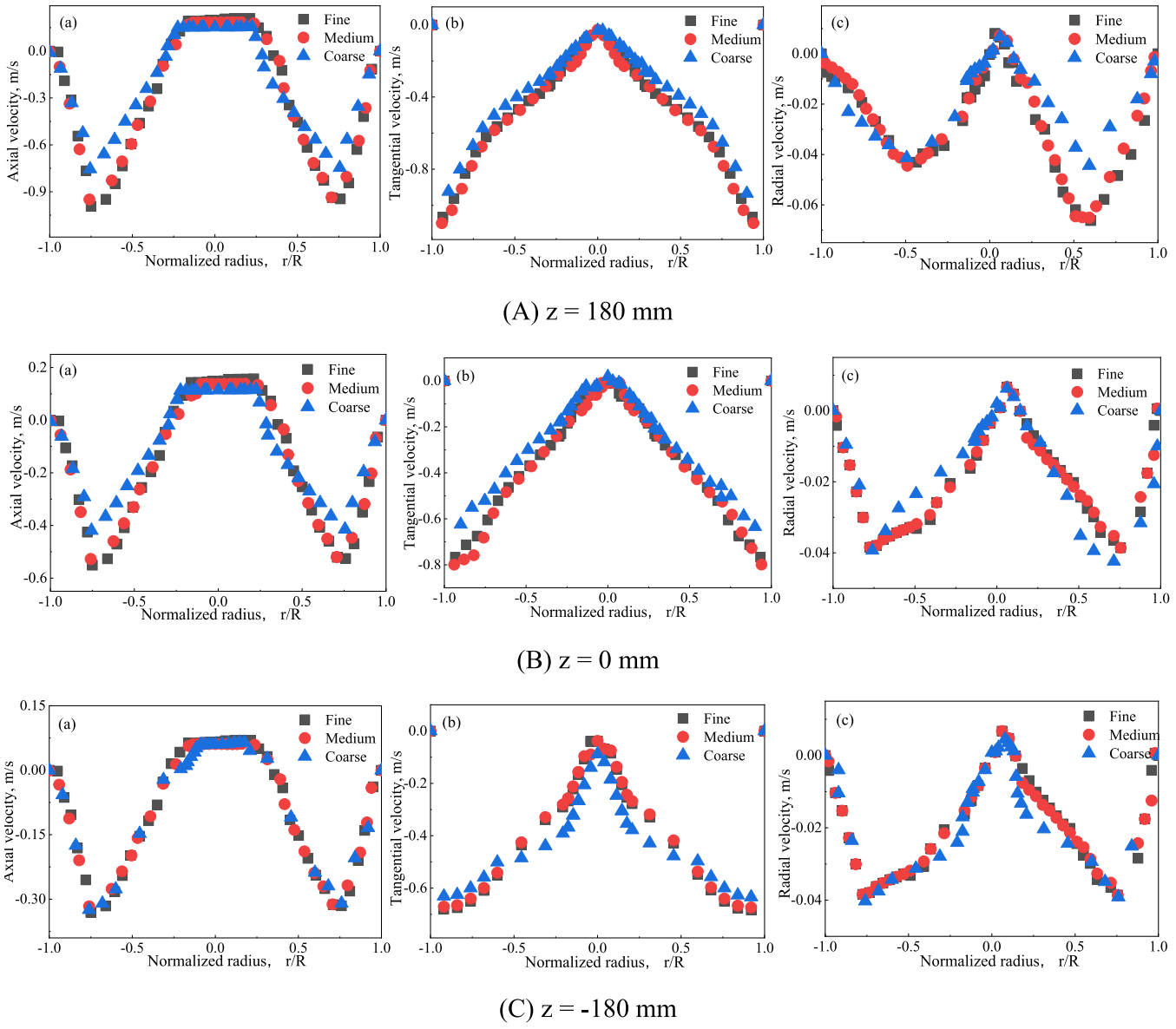

Figure 3. Comparison of numerical simulation velocity under different grid conditions (A) z = 180 mm, (B) z = 0 mm, (C) z = −180 mm, (a) axial velocity, (b) tangential velocity, and (c) radial velocity).

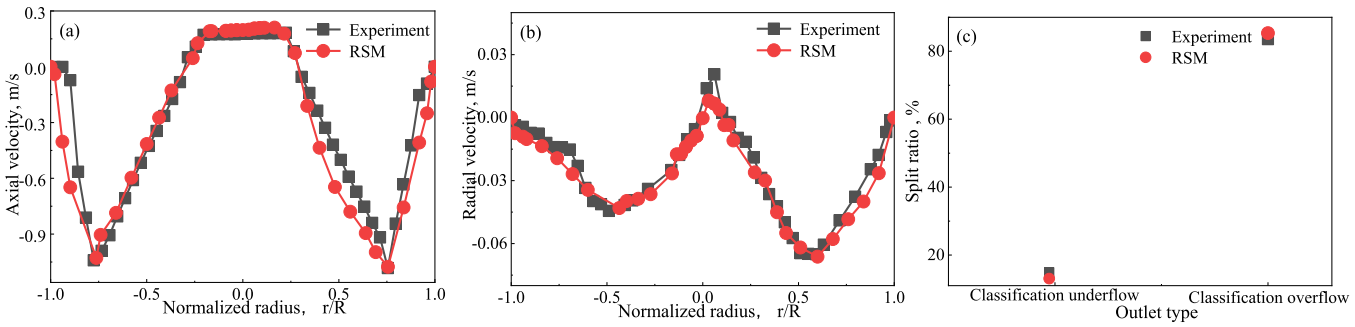

Figure 4. Velocity distribution and split ratio between experiment and simulation ((a) axial velocity, (b) radial velocity, and (c) split ratio).

s[3]), and their calculation formulas are shown in eqs 10−12, respectively. I less than 1% is low turbulent intensity, 1∼10% is medium turbulent intensity, and greater than 10% is high turbulent intensity.[29]

$$I = 0.16Re_f^{-0.125} \tag{10}$$

$$\frac{\partial}{\partial t}(\rho k) + \frac{\partial}{\partial x_i}(\rho k u_i) = \frac{\partial}{\partial x_j}\left[(\mu + \mu_t)\frac{\partial k}{\partial x_j}\right] + \frac{1}{2}(P_{ii} + G_{ii}) - \rho\varepsilon \tag{11}$$

https://doi.org/10.1021/acsomega.2c04168
ACS Omega 2022, 7, 38660−38673

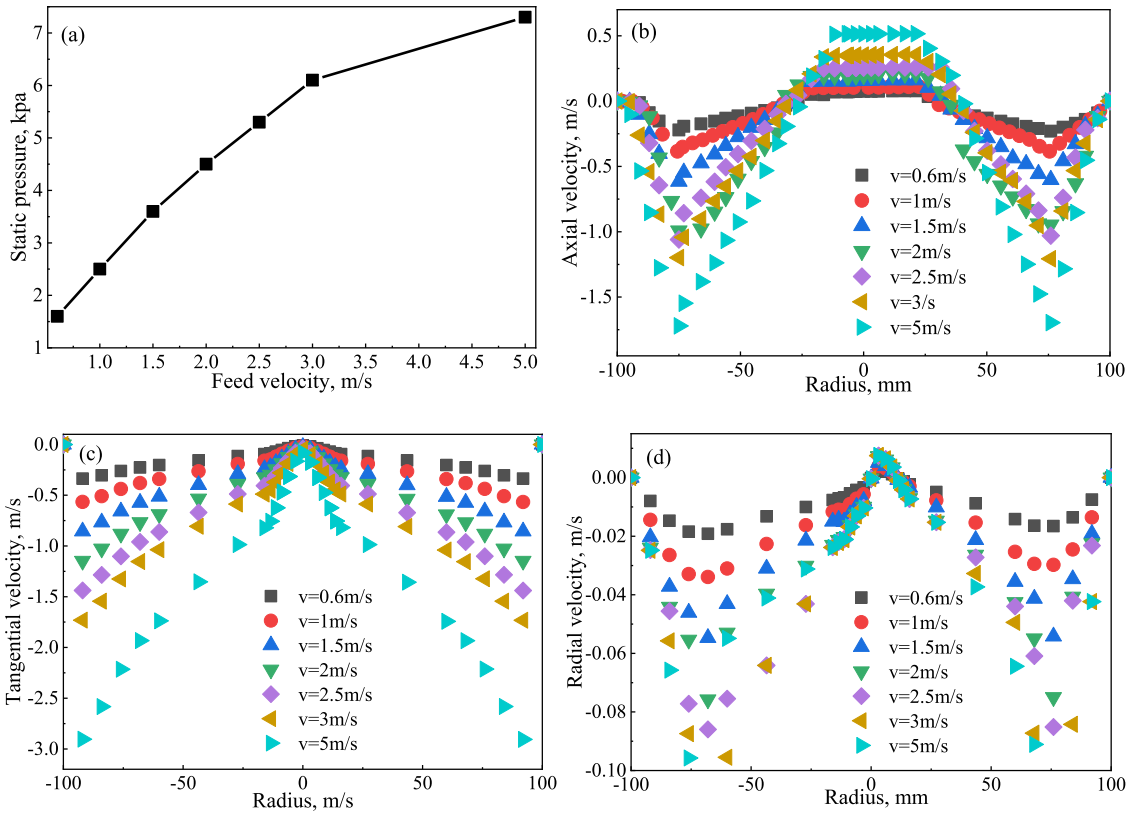

Figure 5. Static pressure and velocity vector distribution of WNT in z = 180 mm under different feed velocities ((a) static pressure, (b) axial velocity, (c) tangential velocity, and (d) radial velocity).

$$\frac{\partial}{\partial t}(\rho\varepsilon) + \frac{\partial}{\partial x_i}(\rho\varepsilon u_i) = 0.72P_{ii}\frac{\partial}{\partial x_j}\left[(\mu + \mu_t)\frac{\partial\varepsilon}{\partial x_j}\right]\frac{\varepsilon}{k} - 1.92\rho\frac{\varepsilon^2}{k} \quad (12)$$

In the CFD simulation of the WNT, the velocity inlet and pressure outlet were adopted as boundary types of feed entrance and product exits, respectively. The feed velocity was 2 m/s, while the pressure out was equal to 1 standard atmospheric pressure. The characteristic size of the inlet is the hydraulic diameter. The SIMPLEC scheme based on the pressure−velocity coupling algorithm was chosen as the solution method. The air volume fraction of 1 in all zones was initialized based on the standard initialization. The size and number of time steps were 0.001 and 20,000, respectively. The max iteration step in each time step was 20. The residual criteria for the convergence are set to 1.0×10^{-8} for all cases.

RESULTS AND DISCUSSION

Validation. *Grid Independence Test.* In order to minimize the uncertainty of input factors, in the numerical simulation, except for the above three kinds of grids, the other conditions (such as the feed velocity of 2 m/s) remained unchanged. The RSM turbulence model and second order precision solver were selected.

Figure 3 displays the distribution of fluid flow velocity: (a) axial velocity, (b) tangential velocity, and (c) radial velocity on different radii at different vertical heights (A) z = 180 mm (cylinder), (B) z = 0 mm (the interface between the cylinder and the cone), and (C) z = −180 mm (cone) in the y = 0 plane of the WNT under three grid specifications. Among them, the radial position was normalized, defined the current radial coordinate (r/R) as the radial radius position (r) divided by the cylindrical radius (R) of the WNT, and the value range of r/R is −1 to 1.

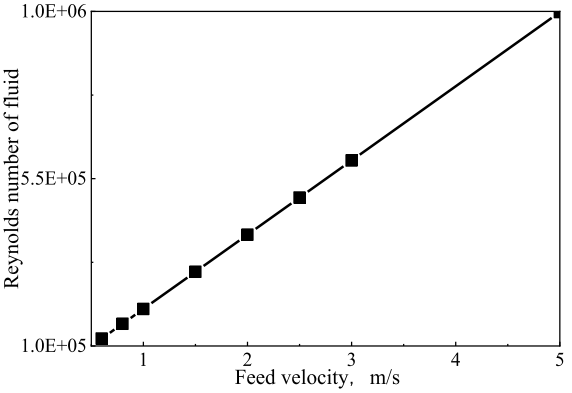

Figure 6. Reynolds number of fluid under different feed velocities.

Figure 3 clearly shows that when the grid densities are kept at the fine and medium levels, the velocity distribution of the flow field is very close, and no obvious differences are evident. Conversely, when the grid level drops to coarse, the simulation results show an obvious difference, and this means that fine and medium grid densities can obtain grid independent solutions. In order to ensure the reliability of the simulation results, the fine density grid is employed in the subsequent numerical simulation of the flow field.

Model Validation. The development process of the WNT flow field was investigated by combining the simulation and experiment methods. The flow field photographed by PIV was

https://doi.org/10.1021/acsomega.2c04168
ACS Omega 2022, 7, 38660−38673

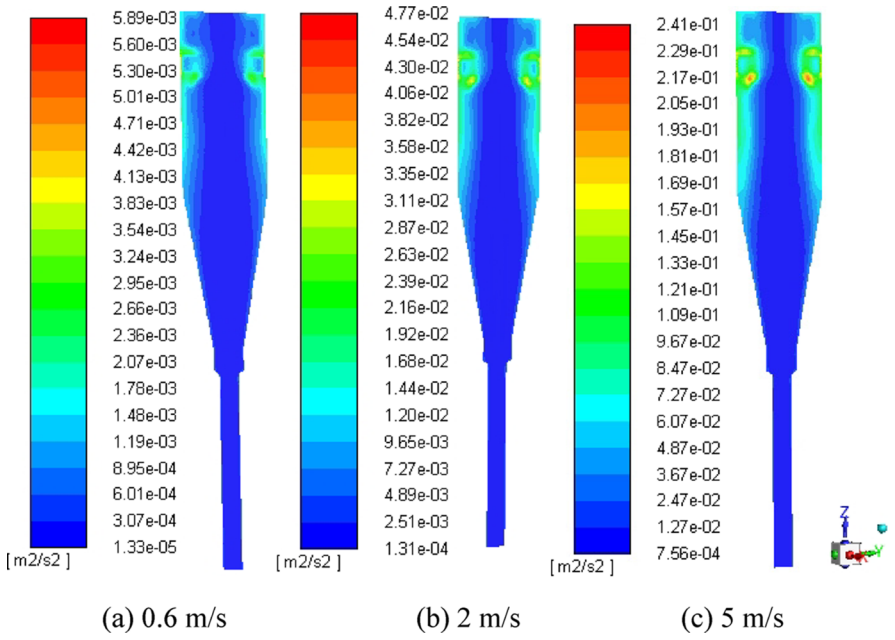

Figure 7. Turbulent kinetic energy k distribution under different feed velocities ((a) 0.6 m/s, (b) 2 m/s, and (c) 5 m/s).

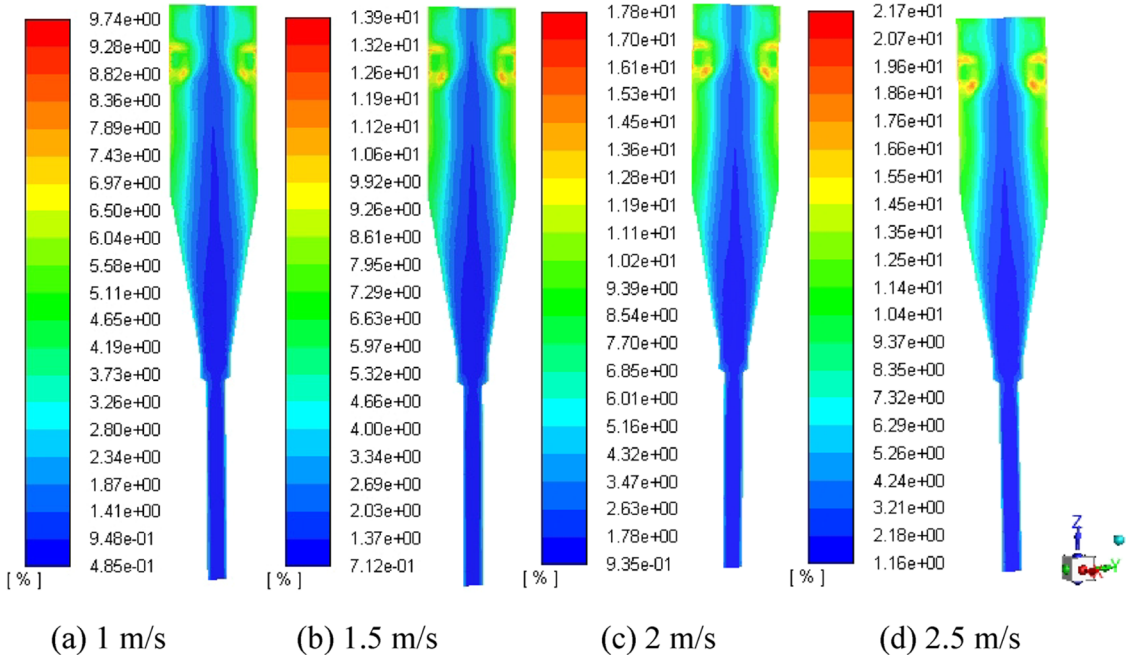

Figure 8. Turbulent intensity I distribution under different feed velocities ((a) 1 m/s, (b) 1.5 m/s, (c) 2 m/s, and (d) 2.5 m/s).

analyzed from the aspects of axial and radial velocities and then compared with the simulation results to verify the reliability of the numerical model. The details are shown in Figure 4a,b, while the experimental and simulated split ratios of classification overflow and underflow are shown in Figure 4c. The feed velocity was controlled at 2 m/s, and then the WNT was run for approximately 30 min to ensure stable system operation. Then, three sets of samples (feed, classification underflow, and classification overflow) were taken in five-minute intervals (at 30, 35, and 40 min) to obtain the representative samples.

The radial position was normalized, defined the current radial coordinate (r/R) as the radial radius position (r) divided by the cylindrical radius (R) of the WNT, and the value range of r/R is −1 to 1.

As shown in Figure 4a,b, the axial and radial velocity distributions and split ratios of the CFD model used do not completely coincide with the experimental results. However, the deviation is reasonable in consideration of the experimental error and the model uncertainty. Overall, numerical simulation prediction results are in good agreement with the experimental data, indicating that the proposed model can describe the distribution characteristics of the WNT flow field. Figure 4c shows the high accuracy of the proposed model for WNT flow field simulation.

Flow Field Characteristics. The static pressure (measured by a manometer) and velocity vector distribution in z = 180 mm (taking the central position of camera in the PIV experiment as an example) under different feed velocities, COO diameters,

https://doi.org/10.1021/acsomega.2c04168
ACS Omega 2022, 7, 38660−38673

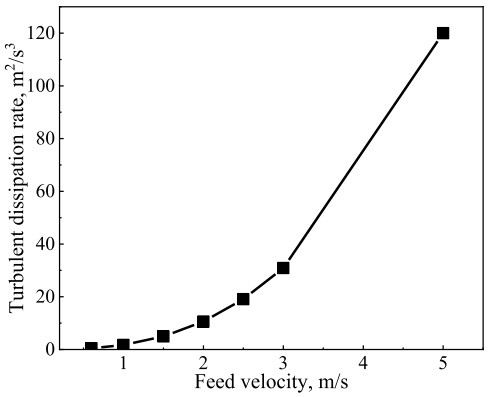

Figure 9. Turbulent dissipation rate ε distribution under different feed velocities.

cone angles, and spigot diameters were analyzed to obtain the pressure and velocity variation characteristics of the flow field. The turbulent kinetic energy k, turbulent intensity I, and turbulent dissipation rate ε under different parameter settings were analyzed to obtain turbulent flow characteristics and provide a reference for the optimization of parameters.

Effect of Feed Velocity on the Flow Field. The feed velocities were selected to be in the range of 0.6−5 m/s (0.6, 1, 1.5, 2, 2.5, 3, and 5 m/s) to ensure a wide practical coverage. When the feed velocity was less than 0.6 m/s, the flow through the COO was extremely small.

Figure 5 refers to the static pressure and velocity vector distribution of WNT in z = 180 mm under different feed velocities: (a) static pressure, (b) axial velocity, (c) tangential velocity, and (d) radial velocity.

Figure 5a shows the rise in static pressure in the flow field with the increase in feed velocity. The fluid passing at the same time increases with the increase in feed velocity, i.e., the feed pressure increases, and the tangential force of the inlet rises. Moreover, the fluid movement is accelerated. As shown in Figure 5b, the velocity decreases and then increases from the wall to the center, and the axial velocity magnitude increases with the increase in feed velocity. Meanwhile, Figure 5c shows that the tangential velocity decreases to the minimum at a radial position and then increases with the rise in radial distance, and the tangential velocity decreases with the increase in feed velocity. As illustrated in Figure 5d, the radial velocity decreases to a peak and then increases with the extension of the radius from the wall to the center, and the radial velocity decreases with the increase in feed velocity. The radial velocity magnitude is much smaller than the axial and tangential velocities.

Figure 6 depicts a significant rise in Re_f of the WNT with the increase in feed velocity. Its order of magnitude is 10^5∼10^6, indicating a turbulent flow in the WNT. Figure 7 presents the kinetic energy distribution. Low (0.6 m/s), medium (2 m/s), and high (5 m/s) feed velocities were chosen to ensure a wide coverage range.

As illustrated in Figure 7, with the rise in feed velocity, the turbulent kinetic energy k significantly increases, and decreases from the cylinder to the cone and from the wall to the center. The max k corresponds to the area near the inlet of the cylinder. The fluid flow in the cylinder represents the turbulent development period, while the turbulent flow in the cone can be regarded as the turbulent decay region.

The turbulent intensity I distribution is shown in Figure 8. Medium (1 and 1.5 m/s) and high (2.5 and 3 m/s) feed velocities were chosen for the analysis of turbulent intensity distribution. Figure 9 shows the turbulent dissipation rate ε under different feed velocities.

Figure 8 also shows that the turbulent intensity I increases significantly with the rise in feed velocity. When the feed velocity is less than or equal to 1 m/s, I is 0% to 10%, and the WNT has low and medium turbulence. When the feed velocity is greater than 1 m/s and less than or equal to 2 m/s, all turbulence types (low, medium, and high turbulence) coexist in the WNT. When the feed velocity is greater than 2 m/s, the turbulence in the WNT is medium and high. I decreases from the cylinder to the cone, and it gradually decreases from the wall to the center. The max I represents the area near the inlet in the cylinder followed by the cylinder, whereas the turbulent intensity in the cone is the lowest. Figure 9 shows the significant increase in turbulent dissipation rate ε with the rise in feed velocity. This trend indicates increasing turbulent kinetic energy loss of the fluid per unit time.

Effect of COO Diameter on the Flow Field. Aiming to investigate the flow field characteristics when the COO diameter is greater than the CUO diameter, a COO diameter in the range of 120∼200 mm was selected in this study (i.e., Ø120, Ø140, Ø160, Ø180, and Ø200 mm).

Figure 10 shows the static pressure and velocity vector distribution of the WNT in z = 180 mm under different COO diameters: (a) static pressure (b) axial velocity, and (c) tangential velocity. Figure 10a shows the decrease in static pressure in the flow field with the increase in COO diameter. This trend can be explained by the gradually increasing contact area between COO and air as the COO diameter increases, resulting in the gradual decrease in internal-external pressure difference in the WNT. Meanwhile, as shown in Figure 10b, the axial velocity decreases to the minimum from the wall to the

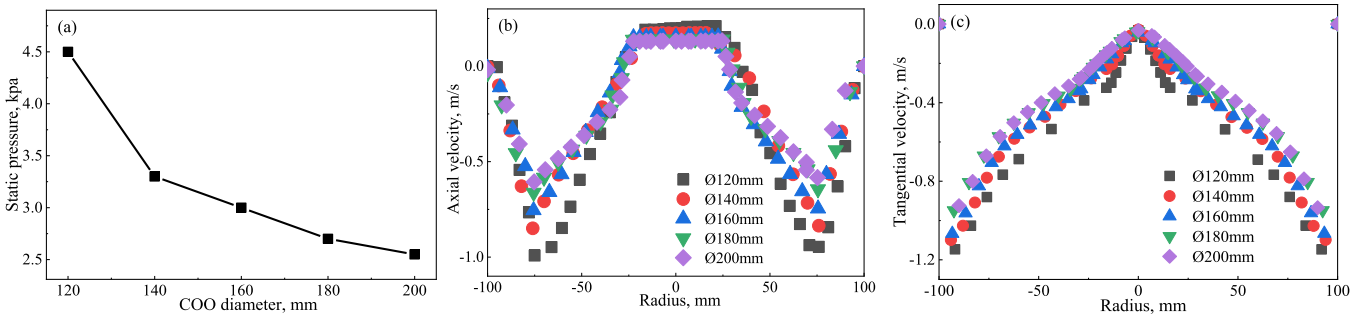

Figure 10. Static pressure and velocity vector distribution of the WNT in z = 180 mm under different COO diameters ((a) static pressure, (b) axial velocity, and (c) tangential velocity).

https://doi.org/10.1021/acsomega.2c04168
ACS Omega 2022, 7, 38660−38673

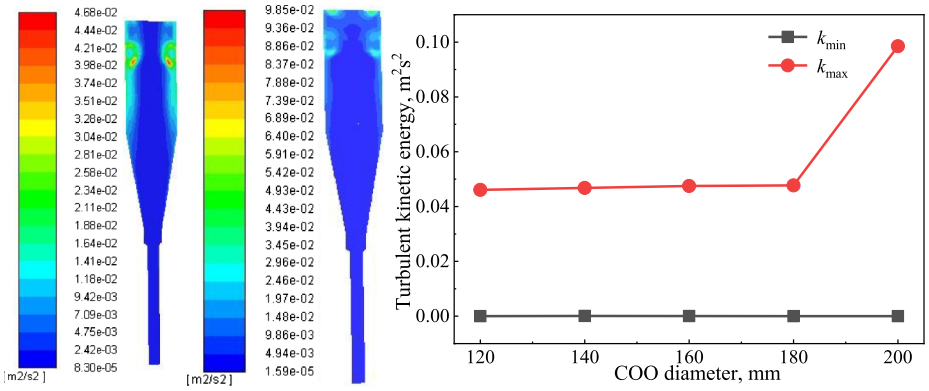

(a) Ø140 mm (b) Ø200 mm (c) k distribution

Figure 11. Turbulent kinetic energy k distribution under different COO diameters ((a) Ø140 mm, (b) Ø200 mm, and (c) k distribution).

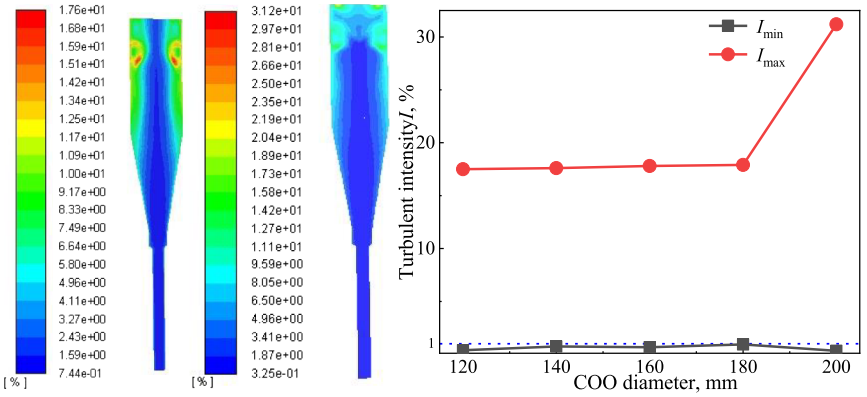

(a) Ø140 mm (b) Ø200 mm (c) I distribution

Figure 12. Turbulent intensity I distribution under different COO diameters ((a) Ø140 mm, (b) Ø200 mm, and (c) I distribution).

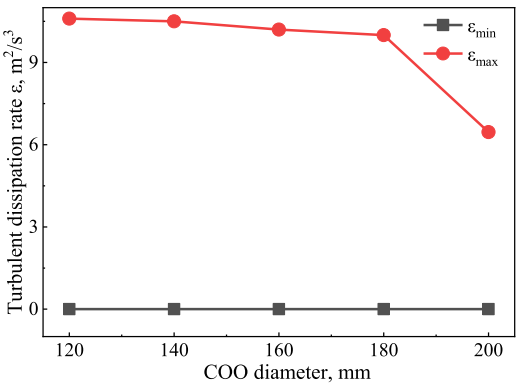

Figure 13. Turbulent dissipation rate ε under different COO diameters.

center, and then it increases. The max axial velocity decreases and the minimum axial velocity increases with the increase in COO diameter. Furthermore, the pressure in the WNT decreases, and the force on the fluid decreases. These phenomena slow down the rising moving speed of the fluid, and more fluid starts to flow out from CUO. Figure 10c shows a similar distribution trend of tangential velocity under different COO diameter settings. As the radial distance increases, the tangential velocity gradually decreases to the minimum and then increases, in other words, the min tangential velocity increases with the rise in COO diameter. The WNT eventually acquires large axial and tangential velocities, which can guarantee the full movement of the fluid in the WNT.

Figures 11, 12, and 13 show the turbulent kinetic energy k, intensity I, and dissipation rate ε under different COO diameter settlings, respectively. Figures 11 and 12 show the rise in turbulent kinetic energy k and turbulent intensity I with the increase in COO diameter. The variation ranges of k and I are extremely small, from Ø120 to Ø180 mm. k and I gradually decrease from the cylinder to the cone and the wall to the center. The max k and I represent the area near the inlet followed by the cylinder, whereas the min k and I represent the cone. However, when the COO diameter is 200 mm, k and I increase rapidly. At this phase, the contact surface between the COO and air can reach the maximum, and strong turbulent movement occurs near the cylinder wall at the COO. The max k and I are transferred from near the inlet to near the cylinder wall at the COO, the k and I gradually decrease from the wall to the center, and the turbulent kinetic energy and intensity near the wall decrease significantly. Figure 12c shows that low, medium, and high turbulence coexist in the WNT.

Figure 13 shows that the turbulent dissipation rate ε decreases with the increase in the COO diameter. The contact surface between the COO and the air increases gradually, the internal and external pressure difference in the WNT decreases with the increase in the COO diameter, as a result, the turbulent dissipation rate ε decreases and the turbulent kinetic energy loss of the fluid per unit time decreases. When the COO diameter is Ø200 mm, the max k and I are near the COO, and the turbulent

https://doi.org/10.1021/acsomega.2c04168
ACS Omega 2022, 7, 38660−38673

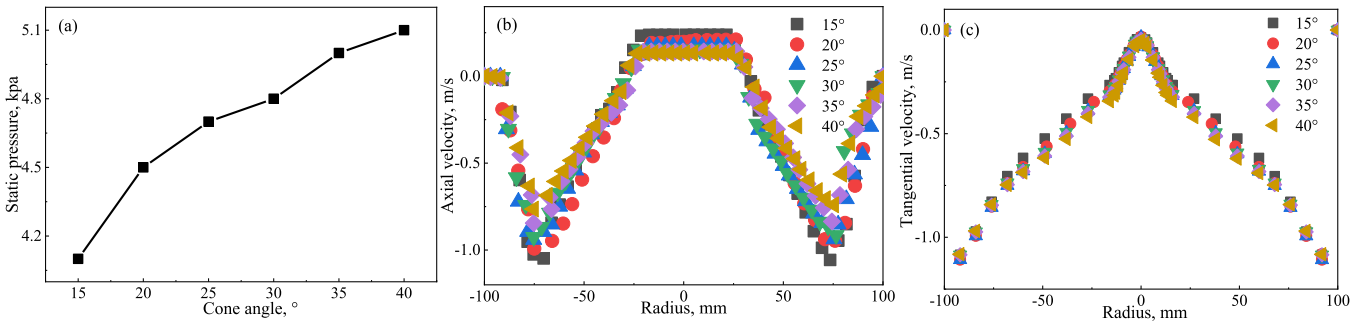

Figure 14. Static pressure and velocity vector distribution of WNT in z = 180 mm under different cone angles ((a) static pressure, (b) axial velocity, and (c) tangential velocity).

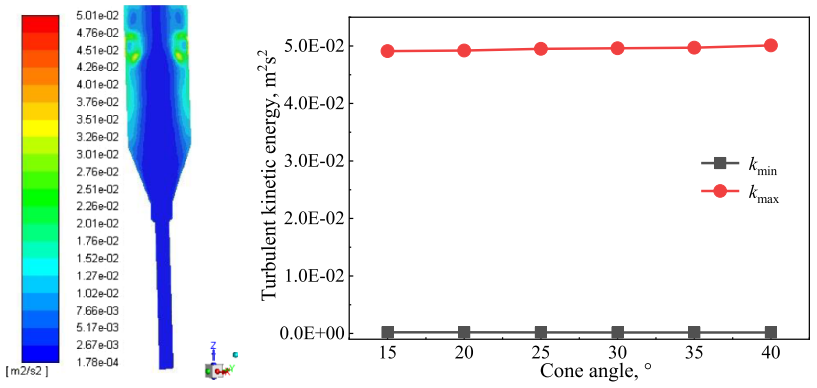

(a) 40° (b) k distribution

Figure 15. Turbulent kinetic energy k distribution under different cone angles ((a) 40°, (b) k distribution).

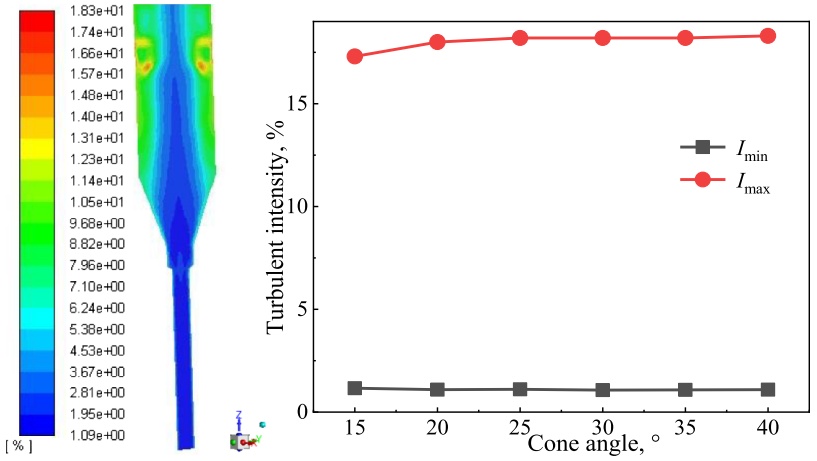

(a) 40° (b) I distribution

Figure 16. Turbulent intensity I distribution under different cone angles ((a) 40°, (b) I distribution).

kinetic energy and intensity near the wall decrease significantly, resulting in the decrease in the turbulent dissipation rate.

Effect of Cone Angle on the Flow Field. Aimed at further investigating the influence of cone angle on the flow field, a wide range of cone angles (15°~40°, in particular, 15°, 20°, 25°, 30°, 35°, and 40°) was investigated in this study.

Figure 14 shows the static pressure and velocity vector distribution of the WNT in z = 180 mm under different cone angles: (a) static pressure (b) axial velocity, and (c) tangential velocity.

Figure 14a shows the rise in static pressure with the increase in the cone angle. The conical height gradually decreases with the increase in the cone angle, the fluid in WNT is squeezed, and the pressure on the fluid increases. Figure 14b shows the symmetrically distributed axial velocity of the flow field. The velocity decreases and then increases from the wall to the center. The max axial velocity decreases and the min axial velocity increases with the increase in cone angle, i.e., the height of the cone section decreases with the increase in cone angle, the motion space and time of the fluid both decrease, and the velocity magnitude of the fluid in z direction decreases.

https://doi.org/10.1021/acsomega.2c04168
ACS Omega 2022, 7, 38660−38673

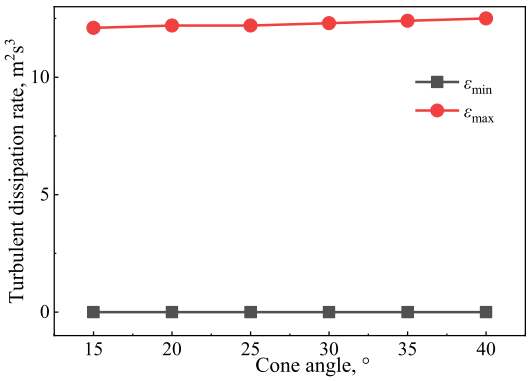

Figure 17. Turbulent dissipation rate ε under different cone angles.

Meanwhile, as shown in Figure 14c, the tangential velocity gradually decreases to the minimum at the radial position and then increases. The change in cone angle has negligible effect on tangential velocity.

By taking 40° as an example, Figures 15 and 16 show the distribution laws of turbulent kinetic energy k and intensity I in combination with the distribution curve. Figure 17 shows the turbulent dissipation rate ε under different cone angles.

Figures 15 and 16 show the increase in turbulent kinetic energy k and intensity I with the increase in cone angle. The variation ranges of k and I are extremely small. k and I gradually decrease from the cylinder to the cone and from the wall to the center. The max k and I represent the area near the inlet followed by the cylinder, while the min k and I represent the cone.

Figure 17 shows the increase in turbulent dissipation rate ε with the increase in cone angle. Furthermore, the conical height decreases, the fluid in WNT is squeezed, and the internal-external pressure difference in the WNT increases. As a result, the turbulent dissipation rate ε and the turbulent kinetic energy loss of the fluid both increase.

Effect of Spigot Diameter on the Flow Field. A wide range of spigot diameters (20∼70 mm, in particular, 20, 30, 40, 50, 60, and 70 mm) was also studied. Figure 18 shows the static pressure and velocity vector distribution of the WNT in z = 180 mm under different spigot diameters: (a) static pressure (b) axial velocity and (c) tangential velocity.

Figure 18a shows the decrease in static pressure in the flow field with the increase in spigot diameter. In other words, with the increase in spigot diameter, the length of the conical section gradually diminishes, and the contact area between CUO and air gradually increases, resulting in the decrease in internal-external pressure difference in the WNT. Figure 18b shows the gradual decrease in static pressure with the increase in spigot diameter. The rising speed of the fluid slows down, the force on the fluid decreases, and the fluid from CUO increases, resulting in the decrease in the max and min axial velocities. Meanwhile, as illustrated in Figure 18c, the tangential velocity distribution under different spigot diameter settings is symmetrical. The tangential velocity decreases to the minimum and then increases from the wall to the center. The change in tangential velocity is negligible when the spigot diameter is increased.

By taking Ø70 mm as an example, Figures 19 and 20 show the distribution laws of turbulent kinetic energy k and intensity I in combination with the distribution curve. Figure 21 shows the turbulent dissipation rate ε under different spigot diameters.

As illustrated in Figures 19 and 20, the turbulent kinetic energy k and intensity I first decrease and then increase with the rise in spigot diameter, but their variation ranges are extremely small. Furthermore, the contact area between the CUO and air increases, eventually leading to a decrease in k and I. However, when the spigot diameter is greater than 50 mm, the contact area between CUO and air further increases, and the air entering the WNT further increases, causing k and I in the WNT to increase. Then, k and I decrease from the cylinder to the cone and from the wall to the center. The max k and I represent the area near the inlet followed by the cylinder, whereas k and I in the cone are the smallest. Figure 20b shows the coexisting medium and high turbulence in the WNT.

As shown in Figure 21, the turbulent dissipation rate ε first decreases and then increases with the increase in spigot diameter, and it reaches the minimum when the spigot diameter is 50 mm. With the further increase in spigot diameter, the ε increases because of the influence of air, but the variation range of ε is extremely small.

CONCLUSIONS

This study designed a new WNT to solve the problem of depending only on a single gravity settlement of the thickener. The reliability of simulation results was verified by means of simulation (RSM and VOF models) and experiment (PIV). Moreover, the pressure and velocity variation characteristics and turbulent characteristics under different feed velocity, COO diameter, cone angle, and spigot diameter settings were studied to provide the basis for WNT optimization. The key results can be summarized as follows.

(1) With the increase in feed velocity, the static pressure increases, the axial, tangential, and radial velocities decrease and then increase from the wall to the center, and the axial velocity magnitude increases. The Re_f order

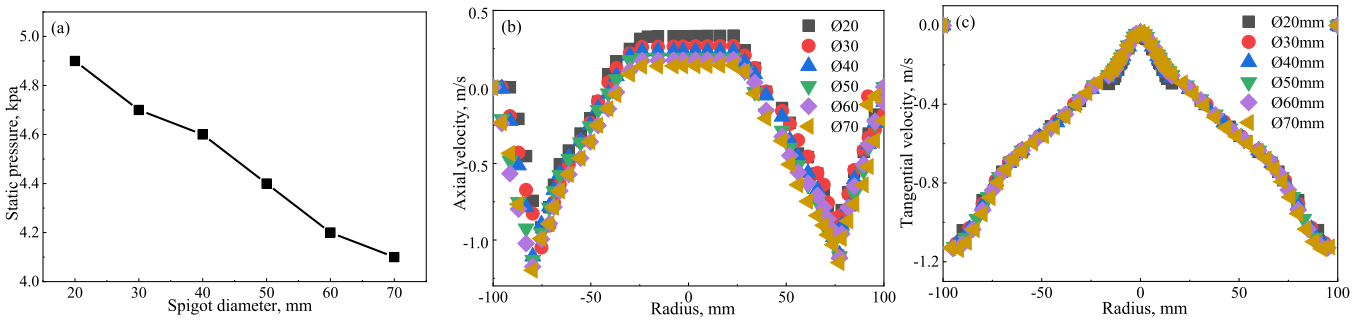

Figure 18. Static pressure and velocity vector distribution of the WNT in z = 180 mm under different spigot diameters ((a) static pressure, (b) axial velocity, and (c) tangential velocity).

https://doi.org/10.1021/acsomega.2c04168
ACS Omega 2022, 7, 38660−38673

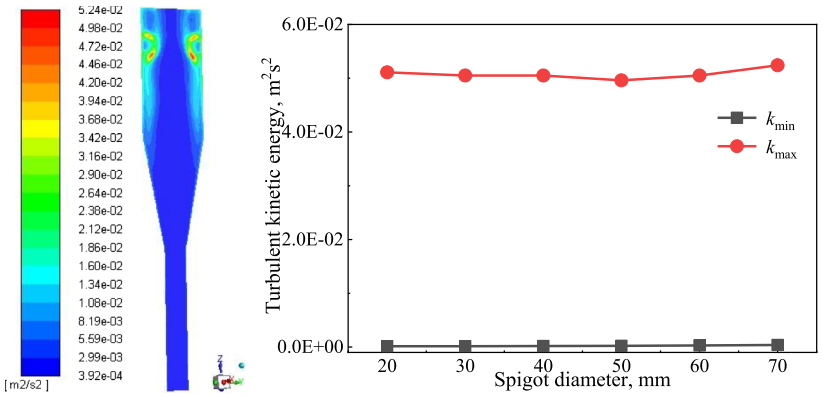

(a) Ø70 mm (b) k distribution

Figure 19. Turbulent kinetic energy k distribution under different spigot diameters ((a) Ø70 mm, (b) k distribution).

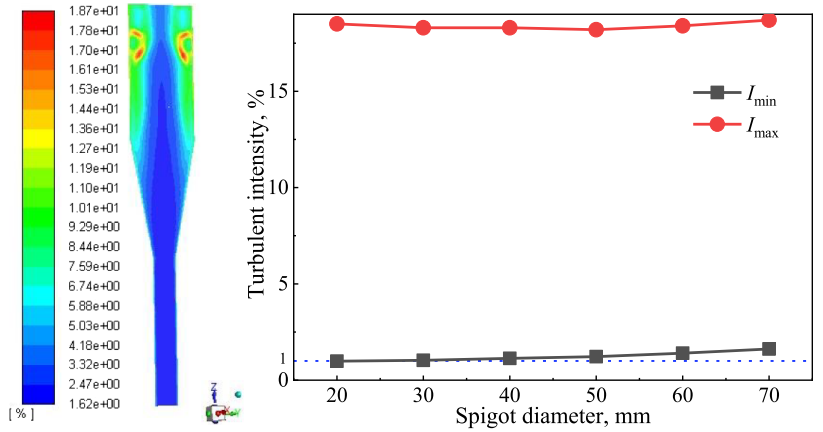

(a) Ø70 mm (b) I distribution

Figure 20. Turbulent intensity I distribution under different spigot diameters ((a) Ø70 mm, (b) I distribution).

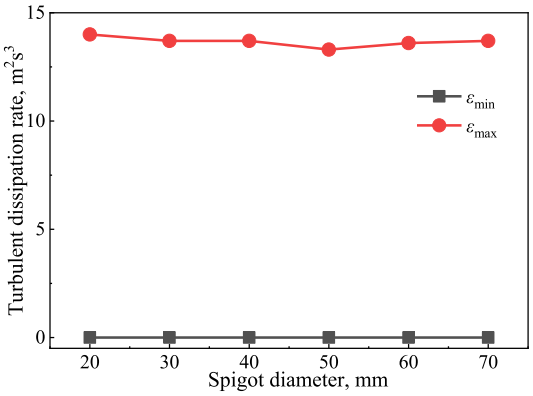

Figure 21. Turbulent dissipation rate ε under different spigot diameters.

of magnitude is 10^5~10^6. The turbulent kinetic energy k, intensity I, and turbulent dissipation rate ε all increase significantly. k and I decrease from the cylinder to the cone and from the wall to the center, and the max k and I represent the area near the inlet. Low and medium turbulence exists in the WNT from 0.6 to 1 m/s; low, medium, and high turbulence coexist in the WNT greater than 1 to 2 m/s; and medium and high turbulence exist in the WNT greater than 2 to 5 m/s.

(2) With the increase in COO diameter, the static pressure decreases, the max axial velocity decreases, and the minimum axial velocity increases. The tangential velocity gradually decreases to the minimum and then increases from the wall to the center, and the min tangential velocity increases. The turbulent kinetic energy k and turbulent intensity I both increase. The variation ranges of k and I are extremely small from Ø120 to Ø180 mm. k and I gradually decrease from the cylinder to the cone and from the wall to the center. The max k and I represent the area near the inlet followed by the cylinder, and the min k and I represent the cone. When the COO diameter is 200 mm, k and I increase rapidly, the max k and I are transferred from near the inlet to near the cylinder wall at the COO, and the k and I near the wall decrease significantly. The turbulent dissipation rate ε decreases with the increase in COO diameter.

(3) With the increase in cone angle, the static pressure increases, the max axial velocity decreases, and the min axial velocity increases. The tangential velocity gradually decreases to the minimum and then increases from the wall to the center. The turbulent kinetic energy k and intensity I both increase. k and I gradually decrease from the cylinder to the cone and from the wall to the center. The max k and I represent the area near the inlet followed by the cylinder, and the min k and I represent the cone.

https://doi.org/10.1021/acsomega.2c04168
ACS Omega 2022, 7, 38660−38673

The turbulent dissipation rate ε increases with the rise in cone angle.

(4) With the increase in spigot diameter, the static pressure decreases, the axial velocity decreases, and the tangential velocity decreases to the minimum and then increases from the wall to the center. The turbulent kinetic energy k and intensity I decrease and then increase, and they decrease from the cylinder to the cone and from the wall to the center. The max k and I represent the area near the inlet followed by the cylinder, and the k and I in the cone are the smallest. Furthermore, medium and high turbulence exists in the WNT. The turbulent dissipation rate decreases and then increases with the increase in spigot diameter.

AUTHOR INFORMATION

Corresponding Author

Fanfei Min − *School of Materials Science and Engineering, Anhui University of Science and Technology, Huainan 232001, China;* orcid.org/0000-0001-9161-745X; Email: ffmin@aust.edu.cn

Authors

Yan Zheng − *School of Materials Science and Engineering, Anhui University of Science and Technology, Huainan 232001, China;* orcid.org/0000-0001-5176-114X

Chuanzhen Wang − *School of Materials Science and Engineering, Anhui University of Science and Technology, Huainan 232001, China; State Key Laboratory of Mining Response and Disaster Prevention and Control in Deep Coal Mines, Anhui University of Science and Technology, Huainan 232001 Anhui, China*

Complete contact information is available at: https://pubs.acs.org/10.1021/acsomega.2c04168

Notes

The authors declare no competing financial interest.

ACKNOWLEDGMENTS

This work was supported by the Key Research and Development Plan of Anhui Province, China (Grant No. 202004a07020044) and the National Natural Science Foundation of China (Grant No. 51874011).

REFERENCES

(1) Gheshlaghi, M. E.; Goharrizi, A. S.; Shahrivar, A. A. Simulation of a semi-industrial pilot plant thickener using CFD approach. *Int. J. Min. Sci. Technol.* **2013**, *23*, 63−68.

(2) Song, X. Z.; Xu, Z. M.; Li, G. S.; Pang, Z. Y.; Zhu, Z. P. A new model for predicting drag coefficient and settling velocity of spherical and non-spherical particle in Newtonian fluid. *Powder Technol.* **2017**, *321*, 242−250.

(3) Mohanarangam, K.; Hopkins, J.; Simic, K.; Stephensc, D. W.; Fawell, P. D. Turbulent mixing of concentrated viscoelastic polymer solution: Influence of submerged sparge shape and orientation. *Miner. Eng.* **2018**, *128*, 1−16.

(4) Wang, X.; Cui, B. Y.; Wei, D. Z.; Song, Z. G.; He, Y.; Bayly, A. E. CFD simulation of tailings slurry thickening in a gravity thickener. *Powder Technol.* **2021**, *392*, 639−649.

(5) Concha, F.; Segovia, J. P.; Vergara, S.; Pereira, A.; Elorza, E.; Leonelli, P.; Betancourt, F. Audit industrial thickeners with new on-line instrumentation. *Powder Technol.* **2017**, *314*, 680.

(6) Cui, B. Y.; Wang, X. T.; Zhao, Q.; Liu, W. G. Study on the degradation of sodium diethyldithiocarbamate (DDTC) in artificially prepared beneficiation wastewater with sodium hypochlorite. *J. Chem.* **2019**, *2019*, No. 7038015.

(7) Langlois, J. I.; Cipriano, A. Dynamic modeling and simulation of tailing thickener units for the development of control strategies. *Miner. Eng.* **2019**, *131*, 131−139.

(8) Rudman, M.; Paterson, D. A.; Simic, K. Efficiency of raking in gravity thickeners. *Int. J. Miner. Process.* **2010**, *95*, 30−39.

(9) White, R. B.; Nguyen, T. V. Fluid flow in thickener feedwell models. *Miner. Eng.* **2003**, *16*, 145−150.

(10) Wong, S. S.; Teng, T. T.; Ahmad, A. L.; Zuhairi, A.; Najafpour, G. Treatment of pulp and paper mill wastewater by polyacrylamide (PAM) in polymer induced flocculation. *J. Hazard. Mater.* **2006**, *135*, 378−388.

(11) Aslan, N.; Shahrivar, A. A.; Abdollahi, H. Multi-objective optimization of some process parameters of a lab-scale thickener using grey relational analysis. *Sep. Purif. Technol.* **2012**, *90*, 189−195.

(12) Du, J.; Mcloughlin, R.; Smart, R. Improving thickener bed density by ultrasonic treatment. *Int. J. Miner. Process.* **2014**, *133*, 91−96.

(13) Schwarz, R. CFD modelling of thickeners at Worsley Alumina Pty Ltd. *Appl. Math. Model.* **2002**, *26*, 281−296.

(14) Rudman, M.; Simic, K.; Paterson, D. A.; Strode, P.; Brent, A.; Šutalo, I. D. Raking in gravity thickeners. *Int. J. Miner. Process.* **2008**, *86*, 114−130.

(15) Gladman, B. R.; Rudman, M.; Scales, P. J. Experimental validation of a 1-D continuous thickening model using a pilot column. *Chem. Eng. Sci.* **2010**, *65*, 3937−3946.

(16) Nguyen, T. V.; Farrow, J. B.; Smith, J.; Fawell, P. D. Design and development of a novel thickener feedwell using computational fluid dynamics. *J. South. Afr. Inst. Min. Metall.* **2012**, *112*, 105−119.

(17) Randjic, D. Proposition of new indices and parameters for grain size classification efficiency estimation. *J. Min. Metall.* **2008**, *44A*, 17−23.

(18) Jeldres, R. I.; Concha, F.; Toledo, P. G. Population balance modelling of particle flocculation with attention to aggregate restructuring and permeability. *Adv. Colloid Interface Sci.* **2015**, *224*, 62−71.

(19) Farrow, J. B.; Fawell, P. D.; Johnston, R. R. M.; Nguyen, T. B.; Rudman, M.; Simic, K.; Swift, J. D. Recent developments in techniques and methodologies for improving thickener performance. *Chem. Eng. J.* **2000**, *80*, 149−155.

(20) Rahimi, M.; Abdollahzadeh, A. A.; Rezai, B. Dynamic simulation of tailing thickener at the Tabas coal washing plant using the phenomenological model. *Int. J. Miner. Process.* **2016**, *154*, 35−40.

(21) Vieira, L. G. M.; Barrozo, M. A. S. Effect of vortex finder diameter on the performance of a novel hydrocyclone separator. *Miner. Eng.* **2014**, *57*, 50−56.

(22) Concha, F.; Burger, R.; Bustos, M. C. Settling velocities of particulate systems: 9. Phenomenological theory of sedimentation processes: numerical simulation of the transient behaviour of flocculated suspensions in an ideal batch or continuous thickener. *Int. J. Miner. Process.* **1999**, *55*, 267−282.

(23) Wu, A. X.; Ruan, Z. E.; Li, C. P.; Wang, S. Y.; Wang, Y.; Wang, J. D. Numerical study of flocculation settling and thickening of whole-tailings in deep cone thickener using CFD approach. *J. Cent. South Univ.* **2019**, *26*, 711−718.

(24) Ruan, Z. E.; Li, C. P.; Shi, C. Numerical simulation of flocculation and settling behavior of whole-tailings particles in deep-cone thickener. *J. Cent. South Univ.* **2016**, *23*, 740−749.

(25) Zhou, T.; Li, M.; Zhou, C. Q.; Zhou, J. M. Numerical simulation and optimization of red mud separation thickener with self-dilute feed. *J. Cent. South Univ.* **2014**, *21*, 344−350.

(26) Banisi, S.; Yahyaei, M. Feed Dilution-Based Design of a Thickener for Refuse Slurry of a Coal Preparation Plant. *Int. J. Coal Prep. Util.* **2008**, *28*, 201−223.

(27) Aashranth, B.; Pandey, N. K.; Anand, V. P.; Panda, S. K. Disengagement of dispersed cerium oxalate from nitric-oxalic acid medium in a batch settler: Measurements and CFD simulations. *Ann. Nucl. Energy* **2020**, *144*, No. 107574.

(28) Zhou, T.; Li, M.; Li, Q. L.; Lei, B.; Chenn, Q. Z.; Zhou, J. M. Numerical simulation of flow regions in red mud separation thickener's feedwell by analysis of residence-time distribution. *Trans. Nonferrous Met. Soc. China* **2014**, *24*, 1117−1124.
(29) Tanguay, M.; Fawell, P.; Adkins, S. Modelling the impact of two different flocculants on the performance of a thickener feedwell. *Appl. Math. Model.* **2014**, *38*, 4262−4276.
(30) Fawell, P. D.; Nguyen, T. V.; Solnordal, C. B.; Stephens, D. W. Enhancing Gravity Thickener Feedwell Design and Operation for Optimal Flocculation through the Application of Computational Fluid Dynamics. *Miner. Process. Extr. Metall. Rev.* **2019**, *42*, 496−510.
(31) Wang, X. T.; Cui, B. Y.; Wei, D. Z.; Song, Z. G.; Hec, Y.; Bayly, A. E. CFD-PBM modelling of tailings flocculation in a lab-scale gravity thickener. *Powder Technol.* **2022**, *396*, 139−151.
(32) Stephens, D. W.; Gorissen, D.; Crombecq, K.; Dhaene, T. Surrogate based sensitivity analysis of process equipment. *Appl. Math. Model.* **2011**, *35*, 1676−1687.
(33) Owen, A. T.; Nguyen, T. V.; Fawell, P. D. The effect of flocculant solution transport and addition conditions on feedwell performance in gravity thickeners. *Int. J. Miner. Process.* **2009**, *93*, 115−127.
(34) Aslan, N.; Cifci, F.; Yan, D. Optimization of process parameters for producing graphite concentrate using response surface methodology. *Sep. Purif. Technol.* **2008**, *59*, 9−16.
(35) Liu, Q. Y.; Liu, H.; Song, J. Optimization of Structural Parameters of Integrated Cyclone for Degassing and Oil Removal. *Mech. Sci. Technol. Aerosp. Eng.* **2020**, *39*, 1691−1697.
(36) Xu, Y. X. Numerical simulation and analysis of the separation process in the hydrocyclone. *East China Univ. Sci. Techno.* **2012**, 1−5.
(37) Wang, B.; Yu, A. B. Numerical study of particle-fluid flow in hydrocyclones with different body dimensions. *Miner. Eng.* **2006**, *19*, 1022−1033.
(38) Zhang, Y. K.; Liu, P. K.; Xiao, L. J.; Yang, X. H.; Yang, J. R. Numerical simulation of multiphase flow inside hydrocyclone based on CFD. *Comput. Modell. New Technol.* **2014**, *18*, 1374−1379.
(39) Wang, C. Z.; Yu, A. H.; Zhu, Z. S.; Liu, H. Z.; Khan, M. S. Mechanism of the absent air column in three products hydrocyclone screen (TPHS): experiment and simulation. *Processes* **2021**, *9*, 431.
(40) Wang, A.; Yan, X. K.; Wang, L. J.; Cao, Y. J.; Liu, J. T. Effect of cone angles on single-phase flow of a laboratory cyclonic-static microbubble flotation column: PIV measurement and CFD simulations. *Sep. Purif. Technol.* **2015**, *149*, 308−314.
(41) Uzi, A.; Halevy, G. B.; Levy, A. CFD-DEM modeling of soluble NaCl particles conveyed in brine. *Powder Technol.* **2020**, *360*, 1278−1294.
(42) Wang, C. Z. Study on characteristics of flow field and mechanism of particles passing through sieve under centrifugal coupled screening effect. *China Univ. Min. Technol.* **2019**, 77−81.

https://doi.org/10.1021/acsomega.2c04168
ACS Omega 2022, 7, 38660−38673